Nanoscale

Accepted Manuscript

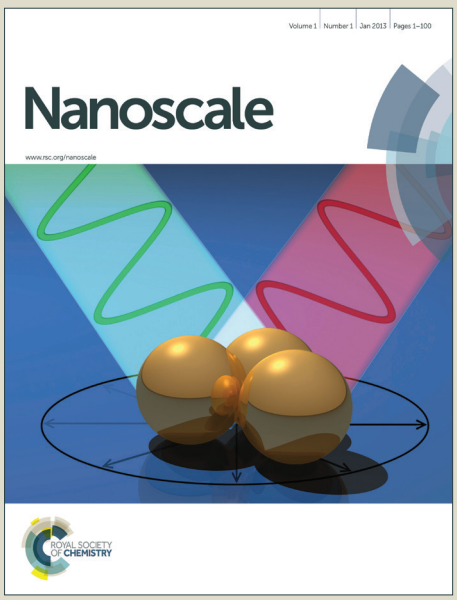

ROYAL SOCIETY OF CHEMISTRY

www.rsc.org/nanoscale

Synthesis and Controllable Oxidation of Monodisperse Cobalt-Doped Wüstite Nanoparticles and their Core-Shell Stability and Exchange-Bias Stabilization

Chih-Jung Chen,[a,b] *Ray-Kuang Chiang,*[*a] *Saeed Kamali,*[*c] *and Sue-Lein Wang*[b]

[a] Nanomaterials Laboratory, Far East University, Hsing-Shih, Tainan 74448, Taiwan

[b] Department of Chemistry, National Tsing Hua University, Hsinchu 30013, Taiwan

[c] MABE Department, University of Tennessee Space Institute, Tullahoma, TN 37388, USA

*Correspondence should be addressed to rkc.chem@msa.hinet.net and skamail@utsi.edu

T.O.C.

Oxidized cobalt-doped wüstite nanoparticles show exchange bias properties with enhanced T_N (> 200 K) and good oxidation-resistant stability.

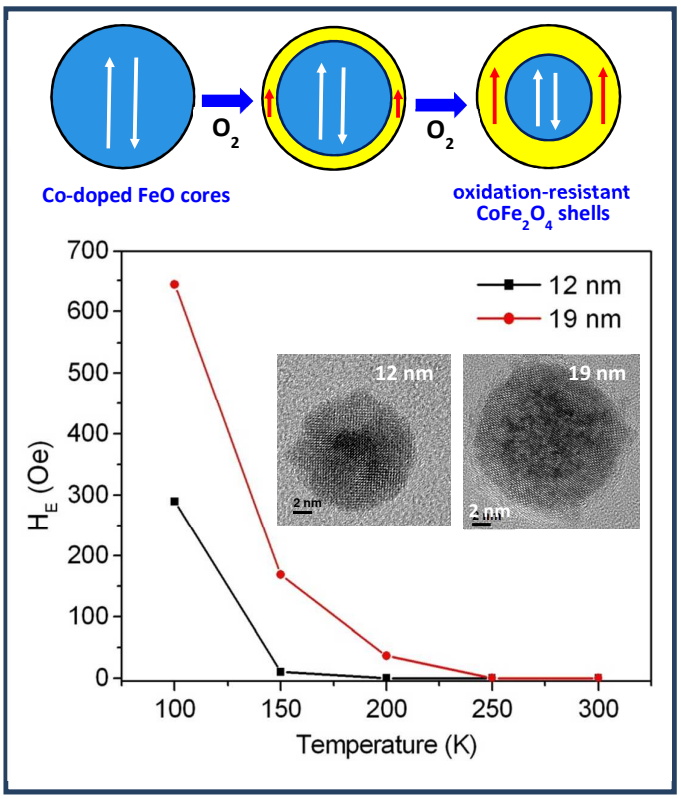

Abstract

Cobalt-doped wüstite (CWT), $Co_{0.33}Fe_{0.67}O$, nanoparticles were prepared via the thermal decomposition of $CoFe_2$-oleate complexes in organic solvents. A controllable oxidation process was then performed to obtain $Co_{0.33}Fe_{0.67}O/CoFe_2O_4$ core-shell structures with different core-to-shell volume ratios and exchange bias properties. The oxidized core-shell samples with a ~4-nm $CoFe_2O_4$ shell showed good resistance to oxygen transmission. Thus, it is inferred that the cobalt ferrite shell provides a better oxidation barrier performance than that of magnetite in the un-doped case. The hysteresis loops of the oxidized 19-nm samples exhibited high exchange bias field (H_E), enhanced coercivity field (H_C), and pronounced vertical shift; thus indicating the presence of a strong exchange bias coupling effect. More importantly, the onset temperature of H_E was found to be higher than 200 K, which suggests that cobalt doping increases the Néel temperature (T_N) of the CWT core. In general, the results show that the homogeneous dispersion of Co in iron precursors improves the stability of the final CWT nanoparticles. Moreover, the $CoFe_2O_4$ shells formed following oxidation increase the oxidation resistance of the CWT cores and enhance their anisotropy energy.

Keywords: monodisperse, nanoparticles, cobalt-doped wüstite, cobalt ferrite, exchange bias

1. Introduction

Magnetic nanoparticles (MNPs)[1] have many interesting core/shell interfacial magnetic interaction properties, including FM (ferromagnetic)/AFM (antiferromagnetic),[2] AFM/FIM (ferrimagnetic),[3] photomagnetic/FM,[4] and FIM(magnetically soft)/FIM(magnetically hard).[5] As a result, they have received extensive attention in the literature for their potential applications in the hyperthermia treatment,[6] magnetic recording,[7] magnetic resonance imaging (MRI),[8] and drug delivery[9] fields. AFM/FIM systems (commonly referred to as inverted exchange bias systems) such as MnO/Mn_3O_4,[3] $Fe_{1-x}O/Fe_3O_4$[10] and $Fe_{1-x}O/CoFe_2O_4$[11] have attracted particular attention due to interesting magnetic proximity effects. Of these various systems, $Fe_{1-x}O$ (wüstite) has a relatively high Néel temperature (T_N) of ~200 K[12] and is easily synthesized. For example, highly monodisperse and large-size (20~100 nm) wüstite NPs can be prepared via the simple decomposition of iron acetylacetonate or iron oleate precursors in organic solvents.[13] Furthermore, the controllable oxidation of wüstite NPs enables the formation of core-shell $Fe_{1-x}O/Fe_3O_4$ NPs with tunable exchange bias properties. Previous studies have shown that the exchange bias properties of core-shell NPs are fundamentally dependent on the core-to-shell volume ratio.[10,14] The interfacial AFM/FIM coupling of core-shell NPs provides an additional source of anisotropy energy, which enhances the magnetization stability of the FIM shell.[12] However, the stabilization effect occurs only at temperatures less than the T_N of the AFM core, where T_N is determined by the core size due to the finite size effect. Furthermore, due to the nonstoichiometry of $Fe_{1-x}O$, which contains a large number of iron vacancies, the AFM/FIM interface does not persist for long since vacancy-assisted diffusion prompts a full transformation to magnetite. In contrast to $Fe_{1-x}O$, CoO has a less defected

rock-salt structure and a higher T_N of ~298 K.[12] Furthermore, magnetic-hard $CoFe_2O_4$ has a higher resistance to oxygen transmission than Fe_3O_4.[15] It is expected that the controllable oxidation of CWT NPs with a Co/Fe ratio of 1:2 will result in the formation of $Co_{0.33}Fe_{0.67}O/CoFe_2O_4$ core-shell NPs with a higher core T_N, an improved resistance toward oxygen transmission, and a greater anisotropy energy.[11] However, this has not been done due to the lack of homogeneous CWT NPs.

M-doped wüstite (M = Co, Mn) NPs have received significant attention in the recent literature due to their relatively higher stability than wüstite and their improved potential for such applications as MR contrast agents[16a] and the catalytic dye decomposition[16b]. Nanoparticles are generally synthesized through the thermal decomposition of a mixture of metal acetylacetonate salts or metal oleate salts.[16] However, the synthesis process invariably yields products with different sizes[16a,16c] and/or compositional homogeneity.[11] Previous studies have shown that the molecular level homogeneity of the precursors is of crucial importance in obtaining products with size and compositional uniformity.[17] Accordingly, in the present study, mixed oleate salts are prepared via the direct and gradual dissolution of bulk Co_3O_4 and goethite powders in oleic acid at a high temperature (295 □) in order to obtain precursors of a uniform size and a homogeneous composition. Monodisperse cobalt-doped wüstite (CWT), $Co_{0.33}Fe_{0.67}O$, NPs with a Co to Fe ratio of 1:2 and dimensions ranging from 7 ~ 19 nm are then synthesized via the decomposition of the $CoFe_2$-oleate precursors in various high boiling point (b.p.) solvents. A controllable oxidation process is then performed to prepare $Co_{0.33}Fe_{0.67}O/CoFe_2O_4$ core-shell NPs with different core-to-shell volume ratios and thus different exchange bias properties. The phase, structure and

temperature-dependent magnetization properties of the various samples are then systematically explored.

2. Experimental Section

Chemicals. Goethite (α-$Fe_2O_3 \cdot H_2O$, 99.9 %, Strem), cobalt oxide (Co_3O_4, 99.9%, Strem), oleic acid (OA, 90 %, Showa), trimethylamine N-oxide dehydrated (98%, Alfa Aesar), 1-hexadecene (HDE, 90 %, Acros, b.p. 305 □), 1-octadecene (ODE, 90%, Acros, b.p. 320 □), and 1-eicosane (ESE, 99%, TCI, b.p. 340 □) were used in the as-received condition without further purification.

Synthesis of $CoFe_2$-oleate complexes. Co_3O_4 (4 mmol), α-$Fe_2O_3 \cdot H_2O$ (12 mmol), and OA (156 mmol) were mixed in a 100 mL three-necked round-bottom flask and heated to 295 □ at a rate of 15 □/min under a flow of N_2. Note that the amount of OA was set as 1.5 times of equivalent to ensure the efficient dissolution of the bulk oxide powders.[18] During the reaction process, the reactant bubbled vigorously and spilled out of the flask as a result of water generation. Moreover, the color of the bulk oxide mixture gradually changed to brown as the reaction proceeded. The change in color was consistent with the disappearance of the bulk oxide diffraction peaks observed in the sampled aliquot. After 4 h, X-Ray Diffraction (XRD) and Infrared (IR) analyses showed that the bulk oxide was completely dissolved within the fatty acid. The resulting brown grease-like product was allowed to cool to room temperature and was then diluted with a mixture of hexane and acetone (1:20) and centrifuged at a speed of 5000 rpm. Finally, the precipitate was washed with acetone and dried at a temperature of 60 □ for 24 h.

Synthesis of monodisperse CWT NPs. $Co_{0.33}Fe_{0.67}O$ NPs with sizes in the range of 7 ~ 19 nm were synthesized by decomposing the $CoFe_2$-oleate in different high b.p. solvents and different amounts of OA (see Table 1). In a typical reaction (see run 2 in Table 1), a mixture of $CoFe_2$-oleate 3 mmol, OA (4 mmol), and ODE (9 mL) was loaded into a 100 mL three-necked round-bottom flask, heated to 320 □ at a rate of 15 □/min under a flow of N_2 gas, and then maintained at this temperature for 120 min. (Note that the temperature was controlled via a heating mantel and a thermocouple positioned above the magnetic stirrer.) During the reaction process, the color of the reactant changed from brown to black as a result of the decomposition of the $CoFe_2$-oleate and the formation of NPs. The resulting product was diluted with hexane and ethanol and was then centrifuged at 5000 rpm. Finally, the precipitate was washed twice in a mixed solvent of hexane/ethanol (volume ratio: 1:4, total volume ~90 mL) to produce a black powder. TEM samples were prepared by dropping a hexane suspension containing the precipitated NPs onto a copper grid (200 meshes) coated with a carbon film. The size of the NPs was determined by averaging the lengths of the major and minor axes of a minimum of 500 different particles using Sigmascan Pro 5 software.

Expedited oxidation of CWT NPs. In the expedited oxidation process, trimethylamine N-oxide dehydrated (6 mmol) was added into as-prepared NP solution at room temperature and then heated to 160 □ at a rate of 20 □/min. The solution was then maintained at this temperature for 20 h under a flow of N_2 gas. Aliquot samples were taken at 1.5, 3, 6 and 20 h for characterization purposes.

Characterization. The phases of the various products were characterized by X-ray powder

diffraction (Shimadzu XRD-6000) using Cu K_α radiation. The IR absorbance properties of the $CoFe_2$-oleate and NPs were analyzed using a Fourier transform infrared spectrometer (FTIR, Nicolet 5700) with a resolution of 4 cm^{-1}. Elemental analyses were carried out using a high-resolution ICP-MS (HR-ICP-MS, Element 2, Thermo-Fisher) and an Elemental Analyzer (Heraeus Vario EL III, Elementar). The products were observed using a transmission electron microscope (JEOL JEM 1200EX) with an accelerating voltage of 80 kV and a high-resolution transmission electron microscope (HR-TEM, Philips Tecnai G2 F20 or JEOL JEM 2100) with an accelerating voltage of 200 kV. The distribution of the iron and cobalt elements in the core-shell NPs was analyzed by means of energy-dispersive X-ray spectroscopy (EDS). The inorganic content of the dried NP precipitates was determined using a thermogravimetric analyzer (TGA) under a constant flow of N_2 gas and a heating rate of 20 □/min. Mössbauer spectroscopy measurements were obtained in a constant acceleration mode at 10 K using a Janis SVT-400 cryostat with 100 mCi ^{57}Co in Rh at room temperature as the source. The centroid shifts, δ, were evaluated with respect to metallic α–iron at room temperature. Moreover, the spectra were least-square fitted using Recoil software.[19] The temperature-dependent magnetization properties of the samples were measured under field cooling (FC) and zero-field cooling (ZFC) conditions given a magnetic field strength of 100 Oe. The dc magnetization properties of the products were measured at temperatures of 5 or 300 K and magnetic fields ranging from 0 to 5 T using a superconducting quantum interference device (SQUID). The saturation magnetization (M_s) and coercive field (H_c) properties of each sample were obtained at different temperatures. The FC measurements were obtained by cooling the samples

from room temperature to a temperature below the Néel temperature (T_N) in the presence of a magnetic field with an intensity of 5 T. The ZFC measurements were obtained by performing the same cooling process in the absence of a magnetic field.

3. Results and discussion

3.1 Synthesis and stability of CWT NPs.

$CoFe_2$-oleate complexes prepared via a high-temperature oxide dissolution process were used as homogeneous precursors for the preparation of monodisperse CWT NPs. The decomposed products exhibited good size uniformity and a multi-layered hexagonal-close-packed structure (Fig. 1 and Fig. S1). Furthermore, the size of the NPs was effectively controlled by performing the decomposition process using organic solvents with different boiling points (i.e., different decomposition temperatures) and different amounts of oleic acid (see Table 1). For the chosen decomposition conditions, the size of the NPs was found to vary from 7 ~ 19 nm. More specifically, the NP size increased with an increasing decomposition temperature and an increasing oleic acid addition (see runs 3 and 4 in Table 1). An elemental analysis confirmed the presence of cobalt in the CWT NPs and showed the Fe-to-Co ratio to be around 2:1 by ICP in the NP product with a size of 19 nm (Fig. S2). The EDX results showed a similar Fe-Co composition for all of the NP samples (Fig. 2). The XRD patterns of the NP samples were consistent with that of $Fe_{1-x}O$ (JCPDF file no: 46-1312) and CoO (JCPDF file no: 43-1004) (Fig. 3). However, the effects of Co doping are not easily discerned in the XRD results since the two rock-salt (*Fm3m*) structures have very similar lattice parameters (i.e., a = 4.26 Å for CoO and a = 4.24 Å for FeO). The major peaks in the XRD

patterns were indexed as the (111), (200), (220), (311) and (222) planes of the cubic wüstite structure. However, a close inspection of the patterns showed that the peaks were also closely matched with the (311) and (440) planes of the cobalt ferrite standard (i.e., JCPDF file no: 22-1086); particularly in the case of the NP sample with a size of 7 nm. Notably, wüstite and inverse spinel-type cobalt ferrite have similar FCC oxygen sublattices. Therefore, the shifted broad peaks in the XRD pstterns may indicate the presence of ferrite phase arising from surface oxidation of the CWT NPs. It has been reported that the decomposition of the oleate precursor in ODE solvents at high temperature results in a reductive atmosphere which causes the reduction of Fe^{3+} to Fe^{2+} and thus prompts the formation of wüstite phase.[20] The wüstite NPs then gradually transform to ferrite phase via surface oxidation. In the case of small NPs (e.g., those with a size of 7 nm in the present study), the oxidized ferrite phase dominates the NP products due to significant surface oxidation in the workup processes. However, in the larger products, the oxidized shell does not dominate the whole NP and is thus more difficult to identify in the XRD spectra.

The results described above are consistent with those reported in the literature for wüstite NPs. For example, it has been shown that WT NPs with a size of 22 nm fully transform to spinel ferrite under ambient conditions in 120 days. Furthermore, their partially oxidized core-shell intermediates reveal notable exchange bias coupling.[10a] In the present study, 12.5-nm CWT NPs were stored under ambient conditions and sampled after 30 and 120 days in order to compare their structural stability with that of un-doped WT NPs. The corresponding XRD patterns are shown in Fig. S3. Characteristic (311) and (440) peaks of $CoFe_2O_4$ are apparent in both samples. However, a

quantitative evaluation of the relative phase composition in the two samples is impossible due to the similarity of the XRD patterns for CWT and cobalt ferrite, respectively. Consequently, the phase distribution in the sample aged for 120 days was examined using HR-TEM. The HR-TEM images showed the presence of single-crystalline-like lattice fringes (Fig. 4(a)). Nonetheless, the diffraction pattern showed diffraction spots associated with both WT and spinel ferrite phases (Fig. 4(b)). More specifically, the lattice spacing of d_{hkl} = 0.211 nm can be assigned to the {200} form of CWT or the {400} form of $CoFe_2O_4$, while that of d_{hkl} = 0.149 nm can be assigned exclusively to the {440} form of $CoFe_2O_4$. The phase distribution in the 12.5-nm NPs aged for 120 days was examined by means of inverse fast Fourier transform (FFT) images constructed from the respective diffraction points (Fig. 4(c) and (d)). It is seen that the NPs contain a shell with a thickness of approximately 2 nm (Fig. 4(d), based on the lattice fringes of the sole $CoFe_2O_4$ diffraction spot). In other words, only limited surface oxidation of the NP occurs even after 120 days. Thus, the CWTs have a much higher oxidation resistance than un-doped WT NPs (22-nm WT NPs were fully oxidized after 120 days.[10a]). It is thought that the superior oxidation retardation is the result of a more effective diffusion barrier of the cobalt ferrite shell and/or a less-defected CWT core.

3.2 Expedited oxidation of 12.5-nm CWT NPs.

Due to the slow oxidation rate of the CWT NPs under ambient conditions, a stricter oxidation method was performed to expedite the oxidation process in order to obtain samples with different core-shell dimensions and thus different exchange bias properties. Trimethylamine N-oxide dehydrated (TMNO) is an efficient oxidation agent for colloidal oxide NPs dispersed in organic

solvents.[21] For example, using TMNO, WT NPs with dimensions ranging from 20 ~ 60 nm can be fully oxidized into spinel ferrite within several hours.[22] Thus, the present CWT NPs were oxidized using TMNO at a temperature of 160□ for 20 h; with aliquot samples taken for analysis purposes after 1.5 h, 3 h, 6 h and 20 h, respectively. The phase evolution of the CWT NPs during the oxidation process was monitored using XRD, TEM and selected area electron diffraction (SAED) techniques. The XRD patterns are shown in Fig. S4. Remarkably, the NPs failed to transform fully to cobalt ferrite even after 20 h. The microstructures of the samples obtained during the oxidation process were examined using HRTEM (Fig. 5). As shown in Fig. 5(a), (d) and (g), the 3-h and 20-h samples exhibited only a very small change in the particle size after oxidation, i.e., 12.98 ± 0.52 nm for the 3-h sample and 12.94 ± 0.46 nm for the 20-h sample. The HRTEM image of a single as-prepared CWT particle reveals a single-crystal characteristic with uniform contrast (Fig. 5(b)). However, the micrograph contrast varies and reveals a core-shell structure in the 3-h and 20-h samples (Fig. 5(e) and (h)). For both samples, the lattice spacing has a value of d_{hkl} = 0.214 nm, which can be assigned to the {200} form of CWT or the {400} form of $CoFe_2O_4$. Furthermore, a minor interplanar distance of d_{hkl} = 0.296 nm is observed near the edge of the particles in both samples, and can be assigned exclusively to the {220} form of $CoFe_2O_4$. It is noted that the shell thickness is equal to approximately 4 nm in both samples despite the difference in the oxidation time (i.e., 3 h and 20 h). This suggests that a ~4-nm cobalt ferrite shell provides an effective barrier against further oxygen transmission. The SAED images and diffraction ring line scan patterns of the as-prepared and oxidized samples confirm this tendency (Fig. 5(c), (f) and (i)). The line scan pattern

of the as-prepared NPs is consistent with the WT standard (JCPDF No. 461312) (Fig. 5 (c)); indicating that rock-salt phase is the dominant phase. By contrast, the line scan patterns of the 3-h and 20-h samples show the presence of both rock-salt phase and cobalt ferrite phase; with a slight difference in the relative peak intensity ratio in the two cases. (Note that a WT pattern is used as the standard for the cobalt-doped rock-salt structure since no standard CWT pattern is available.) The electron diffraction pattern of a single particle in the 20-h sample was used to further analyze the phase distribution (Fig. S5). The lattice images reconstructed from the {220} diffraction spot of $CoFe_2O_4$ show that $CoFe_2O_4$ is limited only to the outer shell (see inset in Fig. 5(h)). Notably, when dry air was used instead of a N_2 atmosphere in the CWT synthesis process, a complete transformation to $CoFe_2O_4$ was observed. However, when using this method, it is not possible to obtain samples with different degrees of oxidation. Fig. S6 and S7 present the XRD pattern, TEM image, hysteresis loop and temperature-dependent magnetization properties of the 12.5-nm $CoFe_2O_4$ NPs. The hysteresis loop shows an H_C value of 21 kOe, which is consistent with the characteristic high anisotropy energy of cobalt ferrite.

3.3 Expedited oxidation of 19-nm $Co_{0.33}Fe_{0.67}O$ NPs.

The results presented above show that expediting the oxidation of the 12.5-nm CWT NPs prompts the formation of a cobalt ferrite shell with a thickness of ~4 nm. A small core size (~4-5 nm) causes a reduction in the Néel temperature (T_N) due to the finite size effect. Thus, the critical temperature for stabilization of the FIM shell by the AFM core tends to decrease as well. Given that oxidation of the present CWT NPs results in the formation of a ~4-nm shell as an intermediate state,

the oxidation of larger CWT NPs results, intuitively, in a larger core size in the oxidized product. As a result, it is reasonable to assume that T_N approaches the bulk value. Thus, the oxidation of 19-nm CWT NPs can be expected to yield core-shell samples with an improved stability due to a more pronounced exchange bias effect. Figs. 6(a), (b) and (c) present the TEM image, SAED images and line scan patterns of the diffraction rings in a 19-nm CWT NP oxidized for 20 h. It is seen that the results are similar to those presented in the previous section for the 12.5-nm sample. Applying an inverse FFT technique to reconstruct the lattice fringes, the oxidized sample is found to comprise a CWT core with a size of ~12 nm and a $CoFe_2O_4$ shell with a thickness of ~4 nm (Fig. 6(d), (e) and (f)). Notably, the shell thickness is comparable to that of the oxidized 12.5-nm sample, which confirms that a ~4-nm cobalt ferrite shell acts as an effective barrier in suppressing the transmission of oxygen from the surroundings.

3.4 Mössbauer spectroscopy.

To obtain more detailed insights into the structure of the core-shell NPs, the Mössbauer spectra of the 12.5-nm samples were measured after 120 days of ambient oxidation and 20 h of expedited oxidation, respectively (see Fig. 7). The hyperfine parameters extracted from the 10-K measurements including the centroid shift (δ□, quadrupole shift (ε), magnetic hyperfine field (B_{hf}), magnetic hyperfine field distribution (σ), and intensity (*I*) are summarized in Table 2. For both samples, the spectra are fitted with four sub-spectra. For the ambient oxidation sample, the first two spectrum components, i.e., Q_1 and Q_2, have δ values of 0.531 mm/s and 0.577 mm/s, respectively, which are characteristic values for Fe^{3+} in the octahedral site (i.e., B-site) of $CoFe_2O_4$. The third

component, Q_3, has a δ value of 0.335 mm/s, which is consistent with the characteristic value for Fe^{3+} in the tetrahedral site (i.e., A-site) of $CoFe_2O_4$. It is worth mentioning that the attribution of the first two components with higher δ values to the octahedral site and the third component with lower δ value to the tetrahedral site is based on the fact that the Fe-O bonds in the octahedral site is larger than the Fe-O bond in the tetrahedral site, resulting in higher δ values in the octahedral site compared to the tetrahedral site.[23-26] The B_{hf} values for the three components are 52.5 T, 51.3 T and 50.2 T, respectively. The high value of B_{hf} in each case can be attributed not only to the low measurement temperature (10 K), but also to the presence of Co as the nearest neighbors to both the A-site and B-site Fe atoms[27,28]. The final component, Q_4, has a δ value of 1.214 mm/s, which is consistent with that for high-spin Fe^{2+}. Furthermore, the intensity of this broad signal is equal to 24%; indicating that 76% of the sample is oxidized to $CoFe_2O_4$. The intensities of the different Mössbauer components are proportional to the occupancies of Fe atoms in different parts. CDW has four Fe(Co) per unit cell, 4.330 Å, and $CoFe_2O_4$ has 24 Fe(Co) atoms in the unit cell, 8.393 Å, resulting in 1.22 times higher concentration of Fe atoms per unit volume for CDW compared to the concentration for Fe atoms per unit volume in $CoFe_2O_4$. The ratio between the core volume and the shell volume, with taking into account this 1.22 proportionality factor, is proportional to the Mössbauer component intensities, i.e. 24% and 76% in the ambient oxidized sample, and 6% and 94% in the 20-h expedited oxidized sample. A simple calculation shows that for the oxidized 12.5-nm CWT sample, a $CoFe_2O_4$ shell with a thickness of ~ 2.1 nm is formed around the 8.3 nm CWT core. Furthermore, based on the discussion above, for the shell the intensities of component

Q_1, which is the signal from A-site, and Q_2 and Q_3, which are the signals coming from B-site, are 33%, respective 19% and 24%. Normalizing these values is resulted to have 43.4% of the Fe atoms in the A-site and 56.6% of the Fe atoms in the B-site. As we have two Fe atoms in $CoFe_2O_4$, the cation distribution of the shell is $(Co_{0.13}Fe_{0.87})[Co_{0.87}Fe_{1.13}]O_4$. The four sub-spectra of the 20-h expedited oxidation sample have very similar hyperfine parameters to those of the ambient sample. However, the intensity of the Q_4 component is equal to just 6%. In other words, the sample experiences greater oxidation, and has a calculated final core size of around ~5.2 nm and a $CoFe_2O_4$ shell thickness of around ~3.6 nm. However, the cation distribution is identical to that of the ambient oxidation sample. It is worth mentioning that as all of the measurements were obtained at 10 K, there is no sign of collective magnetic excitation (CME)[29,30] or superparamagnetism[31,32] in either sample.

3.5 Magnetic properties.

The preceding results have shown that the 12.5-nm CWT NPs oxidized under ambient conditions for 120 days comprise a ~2-nm $CoFe_2O_4$ shell and an ~8-nm unreacted core, while those oxidized with TMNO at 160□ (3 h or 20 h) consist of a ~4-nm $CoFe_2O_4$ shell and a ~5-nm unreacted core. In addition, the 19.0-nm CWT sample oxidized with TMNO at 160 □ (20 h) also has a ~4-nm $CoFe_2O_4$ shell, but a larger (~12 nm) unreacted core(Table S1). The effects of the various core-shell structures of the different oxidized samples on the exchange bias properties of the CWT NPs were examined by means of magnetic measurements.

In general, the exchange-bias interaction in core-shell structures can be evaluated by means of the H_E, the ΔH_C and the *VS*. The three parameters are derived from FC and ZFC hysteresis loops obtained at various temperatures in accordance with[33]

$$H_E = -(H^+ + H^-)/2, \qquad (1)$$

$$H_C = (H^+ - H^-)/2, \quad (2)$$

$$\Delta H_C = H_{C,\,FC} - H_{C,\,ZFC}, \quad (3)$$

$$VS = -(M^+ + M^-)/2, \quad (4)$$

where H^+ and H^- denote the right and left intercepts of the hysteresis loop on the field axis, while M^+ and + M^- denote the up and down intercepts of the hysteresis loop on the moment axis.

In the present $Co_{0.33}Fe_{0.67}O/CoFe_2O_4$ core-shell NPs, the coupling across the AFM/FIM interface may prompt a horizontal shift in the FC hysteresis loop and frequently accompanied with an a corresponding increase in H_C since the interfacial FIM spins is aligned to the direction of the applied magnetic field during field cooling from a temperature higher than T_N.[33] Since the exchange bias effect can only take place at temperatures lower than the Néel temperature (T_N) of the AFM component, the presence of Co dopant in the wüstite tends to induce a higher T_N since bulk CoO has a T_N value close to room temperature. However, the FIM $CoFe_2O_4$ shell may result in a higher H_C value than that in conventional Fe_xO/Fe_3O_4 NP systems since the magnetic anisotropy energy of bulk $CoFe_2O_4$ (1.8~2.0 $\times 10^6$ erg/cm^3) is 20 times higher than that of bulk Fe_3O_4 (1.1~1.3 $\times 10^5$ erg/cm^3).[33]

3.5.1 Magnetic properties of ambient oxidation samples.

Fig. 8(a)~(c) present the magnetization-temperature (M-T) curves of the 12.5-nm CWT NPs oxidized under ambient conditions for 0 days (as-prepared), 30 days and 120 days, respectively. In general, the blocking temperature, T_B^{SP}, is defined as the temperature corresponding to the peak point of the ZFC curves, where the energy required to change the direction of the magnetic moment of the particles is comparable to the thermal energy.[34] Fig. 8(a) shows the presence of two blocking temperatures at around ~190 K and ~300 K, respectively, in the as-prepared NPs. By contrast, in the oxidized samples, only one blocking temperature is observed, i.e., at 213 K for the 30-day sample and 215 K for the 120-day sample. In other words, the blocking temperature at 300 K disappears following oxidation; indicating that it may originate from the surface spins caused by oxygen vacancies.[35] The relatively low T_B^{SP} of ~190 K in the as-prepared sample is the result mainly of

uncanceled spins of the AFM NPs. As the NPs are oxidized, T_B^{SP} shifts to 213 K or 215 K due to the formation of the thin FIM $CoFe_2O_4$ shell. Fig. 8(d)~(f) present the 300-K and 5-K (ZFC and FC) hysteresis loops of the as-prepared, 30-d and 120-d ambient oxidation NPs, respectively. Note that the maximum magnetic field used in the measurement process is limited to 5 T in order to prevent the formation of a minor hysteresis loop, which might otherwise affect the accuracy of the measured *VS* and H_E values. For the oxidized CWT NPs, the cobalt ferrite shell has a high anisotropy energy and therefore requires a high field to reach magnetic saturation.[36] The M-H curves are not saturated due to the presence of the AFM core and/or the AFM/FIM coupled interface. The 300-K hysteresis loops of all three samples show strong H_C and M_r (Fig. S8), which is a typical characteristic of FM. As mentioned above, this room temperature FM feature is most likely the result of metal spins induced by oxygen vacancies on the NP surface. M_r and H_C both decrease as the oxidation time increases; indicating that once a stable shell of cobalt ferrite forms, the FM feature disappears (Fig. S8). The as-prepared and 30-day samples exhibit only small H_E and ΔH_C values. However, their hysteresis loops have a prominent *VS* characteristic. It has been reported that a large *VS* stems from the fact that the Zeeman energy is less than the strongly-coupled interfacial exchange energy, and hence rotation of the uncompensated AFM spins is unfeasible.[37] In the current case, rotation of the pinned interfacial spins (uncompensated) is suppressed due to their interfacial coupling with the CWT core.[38] The as-prepared sample has an H_E value of just 261 Oe, which suggests the absence of an appreciable cobalt ferrite shell in the early stages of surface oxidation. This observation is consistent with the small value of ΔH_C (i.e., 350 Oe). Compared to the as-prepared sample, the 30-d and 120-d oxidized samples show more prominent ΔH_C values of 1100 Oe and 7496 Oe, respectively. It is noted that ΔH_C increases with an increasing oxidation time. This tendency can be attributed to an increasing thickness of the $CoFe_2O_4$ as the oxidation process proceeds. More specifically, ΔH_C increases since the long-range order of $CoFe_2O_4$ shell become prominent and thus its interaction with unpinned uncompensated spin become more effectively.[39] In general, the results indicate that the AFM core imposes an additional anisotropy energy on the FIM shell, which opposes the dragging force exerted by the applied magnetic field. Note that this observation is

consistent with the oxidation-dependent nature of the H_E values (i.e., 108 Oe for the 30-d sample and 1310 Oe for the 120-d sample).

It is speculated that a transition surface layer is formed in the as-prepared sample, which has a midway structure between CWT and cobalt ferrite. It is further speculated that the residual (uncompensated) spins in this layer are aligned with the field direction under cooling from a temperature higher than the T_N of the CWT NPs (in the paramagnetic state). Substantial portions of these spins are fixed by the AFM core and do not rotate under the applied field below T_N, which results in a vertical shift in the FC hysteresis loop. However, the low H_E value of the as-prepared sample indicates the absence of a sufficient cobalt ferrite shell and hence a negligible H_E. Notably, the as-prepared sample has a high *VS* value of 8.9 emu/g (Fig. 8(d)), which accounts for approximately 50% of the total magnetization. Similar large *VS* values are observed in the 30-d and 120-d samples (i.e., 8.2 emu/g and 11.6 emu/g, respectively), indicating the products of ambient oxidation contains substantial amount of such pinned spins.

3.5.2 Magnetic properties of expedited oxidation samples.

Figures 9(a) and (b) present the M-T curves of the 12.5-nm and 19-nm CWT samples oxidized in TMNO solution for 20 h. The bifurcation temperature of the ZFC and FC curves for the 12.5-nm sample is referred to as the irreversibility temperature (T_{irr} ~290 K),[40] and is larger than the blocking temperature (i.e., T_B^{SP} ~ 230 K). For monodisperse and non-interacting particles, T_B^{SP} should be very close to T_{irr}.[36] The higher value of T_{irr} in the present case is the result mainly of increased dipole interactions arising from the FIM $CoFe_2O_4$ shell. Notably, these dipole interactions also lead to a broad ZFC peak. For the 19-nm sample, the ZFC and FC curves are separated, indicating that the T_B value of the oxidized NPs is higher than room temperature.

Fig. 9(c) and (d) present the 300-K and 5-K (ZFC and FC) hysteresis loops of the 12.5-nm and 19-nm CWT samples following oxidation in TMNO solution for 20 h. For the 12.5-nm sample, the ZFC hysteresis loop at 5 K has H_C and M_S values of 10.4 kOe and 32.0 emu/g, respectively. In addition, the FC hysteresis loop at 5 K shows prominent exchange bias properties. In particular, the

large H_C value of 14.0 kOe indicates a significant anisotropy energy contribution from the thick cobalt ferrite shell. Furthermore, the *VS*, H_E and ΔHc values (i.e., 2.11 emu/g, 4302 Oe and 3694 Oe, respectively, Table S2) are consistent with the presence of both pinned and unpinned spins on the interfaces. The VS is much less than the ambient oxidation sample indicating the presence of smaller amount pinned uncompensated spins. For the 19-nm sample, prominent exchange bias properties are also observed at 5 K, i.e., *VS*, H_E and ΔHc values of 6.3 emu/g, 2500 Oe and 2728 Oe, respectively. However, due to its larger size, the sample has a greater number of pinned spins and hence lower values of H_E and ΔHc. Furthermore, the nonzero H_C value at 300 K indicates that the cobalt ferrite shell induces a ferromagnetic behavior of the oxidized NP at room temperature (T_B^{SP} > 300 K). For a practical application in recording materials, in an inverted exchange bias system such as the present $Co_{0.33}Fe_{0.67}O/CoFe_2O_4$ core-shell NPs, both a sufficiently large shell with a high T_B value, which means a large enough of volume of FIM shell, and a large core with a high T_N value are desired. Thus this implies a larger size of CWT NPs would be a more interesting system to study.

The T_N (or T_B^{EB}) and T_B (or T_B^{SP}) properties of the 12.5-nm and 19-nm CWT NPs oxidized for 20 h in TMNO solution were determined from the temperature-dependent hysteresis loops under FC (5 T) conditions at temperatures ranging from 100 K to 300 K with a step size of 50 K (Fig. S9(a) and (b), respectively). The temperature-dependent H_E and $H_{C,\,FC}$ values were also measured (Fig. 10). Note that T_B^{SP} is defined here as the temperature above which $H_{C,\,FC}$ has a nonzero value. For the 12.5-nm sample, T_B^{SP} is located somewhere between 200 and 250 K, and is thus comparable with the peak value (230 K) observed in the ZFC curve. By contrast, for the 19-nm sample, T_B^{SP} has a value higher than 300 K (Fig. 10 inset). T_B^{EB}, is defined as the temperature above which H_E has a nonzero value. For the 12.5-nm sample, T_B^{EB} has a value between 150 and 200 K. This low value can be attributed to the small size of the AFM core (~5 nm). As described earlier, the oxidized 19.0-nm CWT NP has a core-shell structure consisting of a large unreacted core (~ 12 nm) and a ~4-nm $CoFe_2O_4$ shell. The T_B^{EB} value lies somewhere between 200 K and 250 K. In other words, the H_E onset temperature is increased in the 19-nm sample due to the larger core size. Notably, the

H_E onset temperature is higher than 200 K (i.e., the bulk T_N value of wüstite). In other words, cobalt doping leads to a higher T_N, since the exchange bias only takes place below T_N.

4. Conclusions

This study has presented a simple method for the synthesis of $Co_{0.33}Fe_{0.67}O$ (CWT) NPs with dimensions ranging from 7 ~ 19 nm via the decomposition of $CoFe_2$-oleate in hot organic solvents. In addition, a controllable oxidation process has been performed to obtain $Co_{0.33}Fe_{0.67}O/CoFe_2O_4$ core-shell NPs with different core-to-shell volume ratios. The correlation between the nanostructure of the core-shell NPs and their exchange bias properties has been systematically examined. In general, the results have shown that the formation of a $CoFe_2O_4$ shell with a thickness of ~4 nm is sufficient to suppress further oxygen transmission from the surroundings to the CWT core. Moreover, the additional stabilization energy imparted from the large anisotropic energy of the $CoFe_2O_4$ shell and the AFM/FIM coupled interface results in advantageous magnetic properties, such as a large H_C, a high H_E, and a prominent *VS*. Finally, the onset temperature of H_E in the oxidized 19-nm sample is larger than the T_N value of bulk wüstite, indicating that cobalt doping enhances the core T_N.

Acknowledgment. The authors would like to thank the National Science Council of the Republic of China, Taiwan for financially support.

References.

1. S. Wei, Q. Wang, J. Zhu, L. Sun, H. Lin and Z. Guo, *Nanoscale*, 2011, **3**, 4474.
2. J. Nogués, V. Skumryev, J. Sort, S. Stoyanov and D. Givord, *Phys. Rev. Lett.*, 2006, **97**, 157203.
3. G. Salazar-Alvarez, J. Sort, S. Suriñach, M. D. Baró and J. Nogués, *J. Am. Chem. Soc.* 2007, **129**, 9102.
4. N. Dia, L. Lisnard, Y. Prado, A. Gloter, O. Stéphan, F. Brisset, H. Hafez, Z. Saad, C. Mathonière, L. Catala and T. Mallah, *Inorg. Chem.* 2013, **52**, 10264.
5. (a) Q. Song, and Z. J. Zhong, *J. Am. Chem. Soc.* 2012, **134**, 10182. (b) J. H. Lee, J. T. Jang, J. S. Choi, S. H. Moon, S. H. Noh, J. W. kim, J. G. Kim, I. S. Kim, K. I. Park and J. Cheon,

Nature Nanotechnology, 2011, **6**, 418.

6. S. H. Noh, W. Na, J. T. Jang, J. H. Lee, E. J. Lee, S. H. Moon, Y. Lim, J. S. Shin and J. Cheon, *Nano Lett.*, 2012, **12**, 3716.
7. J. Nogués, J. Sort, V. Langlais, V. Skumryev, S. Suriñach, J.S. Muñoz, M.D. Baró. Physics Reports, *2005*, **422**, 65.
8. T. J. Yoon, H. Lee, H. Shao and R. Weissleder, A*ngew. Chem. Int. Ed.*, 2001, **50**, 4663.
9. J. Chomoucka, J. Drbohlavova, D. Huska, V. Adam, R. Kizek and J. Hubalek, *Pharmacological Res.*, 2010, **62**, 144.
10. (a) C. J. Chen, R. K. Chiang, H. Y. Lai and C. R. Lin, *J. Phys. Chem. C*, 2010, **114**, 4258; (b) X. Sun, N. F. Huls, A. Sigdel and S. Sun, *Nano Lett*, 2012, **12**, 246. (c) A. Lak, M. Kraken, F. Ludwig, A. Kornowski, D. Eberbeck, S. Sievers, F. J. Litterst, H. Weller and M. Schilling, *Nanoscale*, 2013, **5**, 12286.
11. M. I. Bodnarchuk, M. V. Kovalenko, H. Groiss, R. Resel, M. Reissner, G. Hesser, R. T. Lechner, W. Steiner, F. Schäffler and W. Heiss, Small, 2009, 5, 2247.
12. J. Nogués and I. K. Schuller, *J. Mag. Mag. Mater.* 1999, **192**, 203.
13. Y, Hou, Z. Xu, S.Sun, Angew. Chem., Int. Ed., 2007, **46**, 6329.
14. B. P. Pichon, O. Gerber, C. Lefevre, I. Florea, S. Fleutot, W. Baaziz, M. Pauly, M. Ohlmann, C. Ulhaq, O. Ersen, V. Pierron-Bohnes, P. Panissod, M. Drillon and S. Begin-Colin, *Chem. Mater.*, 2011, **23**, 2886.
15. M. Sytnyk, R. Kirchschlager, M. I. Bodnarchuk, D. Primetzhofer, D. Kriegner, H. Enser, J. Stangl, P. Bauer, M. Voith, A. W. Hassel, F. Krumeich, F. Ludwig, A. Meingast, G. Kothleitner, M. V. Kovalenko and W. Heiss, *Nano Lett.*, 2013, **13**, 586.
16. (a)D. Choi, A. Han, J. P. Park, J. K. Kim, J. H. Lee, T. H. Kim and S. W. Kim, Small, 2009, 5, 571;(b)P. Y Lee, H. S. Teng and C. S. Yeh, *Nanoscale*, 2013, **5**, 7558; (c) C. C. Huang, C. N. Chang and C.S. Yeh, *Nanoscale*, 2011, **3**, 4254;(d) C. Hofmann, I. Rusakova, T. Ould-Ely, D. Prieto-Centurión, K. B. Hartman, A. T. Kelly, A. Lüttge and K. H. Whitmire, *Adv. Funct. Mater.* 2008, **18**, 1661.
17. (a) N. Bao, L. Shen, Y, Wang, P. Padhan and A. Gupta, *J. Am. Chem. Soc.*, 2007, **129**, 12374; (b) A. P. Herrera, L. Polo-Corrales, E. Chavez, J. Cabarcas-Bolivar, O. N. C. Uwakweh and C. Rinaldi, *J. Mag. Mag. Mater.*, 2013, **328**, 41; (c) R. Chen, M. G. Christiansen and P. Anikeeva, *ACS Nano*, 2013, **7**, 8990.
18. C. J. Chen, R. K. Chiang and S. L. Wang, *Cryst. Eng. Comm.*, 2013, **15**, 9161.
19. K. Lagarec, D. C. Rancourt, Recoil, Mössbauer Spectral Analysis Software for Windows, 1.0; Department of Physics, University of Ottawa: Canada, 1998.
20. (a) H. T. Hai, H. Kura, M. Takahashi and T. Ogawa, *J. Coll. Interf. Sci.*, 2010, **341**, 194;(b) I. S. Lyubutin, C. R. Lin, Y. V. Korzhetskiy, T. V. Dmitrieva and R. K. Chiang, *J. Appl. Phys.*, 2009, **106**, 034311.
21. C. J. Chen, H. Y. Lai, C. C. Lin, J. S. Wang and R. K. Chiang, *Nanoscale Res. Lett.*, 2009, **4**, 1343.
22. C. J. Chen, R. K. Chiang, J. S. Wang and S. L. Wang, *J. Nanopart. Res.* 2013, **15**, 1845.
23. S. Kamali-M, A. Bergman, G. Andersson, V. Stanciu, and L. Häggström, *J. Phys.:*

Condens. Matter, 2006, **18**, 5807.

24. S. Kamali, L. Häggström, M. Sahlberg, and R. Wäppling, *J. Phys.: Condens. Matter,* 2011, **23**, 055301.
25. B. J. Evans and S. S. Hafner, *J. Appl. Phys.* 1969, **40**, 1411.
26. G. A. Sawatzky, F. Van Der Woude, and A. H. Morrish, *Phys. Rev.* 1969, **187**, 747.
27. M. Artus et al., *J. Phys.: Condens. Matter* 2011, **23**, 506001.
28. F. L. Deepak et al., *J. Phys. Chem.* 2015, **C 119**, 11947.
29. S. Mørup, D. E. Madsen, C. Frandsen, C. R. H. Bahl, and M. F. Hansen. *J. Phys.: Condens. Matter*, 2007, **19**, 213202,.
30. S. Mørup and H. Topsøe. *Appl. Phys.*, 1976, **11**, 63,.
31. S. Kamali-M, T. Ericsson, and R. Wäppling, *Thin Solid Films*, 2006, **515**, 721.
32. L. Häggström, S. Kamali, T. Ericsson, P. Nordblad, A. Ahniyaz, and L. Bergström, *Hyperfine Interact.* 2008, **183**, 49.
33. J. Nogués and I. K. Schuller, *J. Mag. Mag. Mater.* 1999, **192**, 203.
34. D. L. Leslie-Pelecky and R. D. Rieke, *Chem. Mater.* **1996**, *8*, 1770
35. (a) D. P. Dutta, G. Sharma, P. K. Manna, A. K. Tyagi and S. M. Yusuf, *Nanotechnology*, 2008, **19**, 245609; (b) A. Sundaresan, R. Bhargavi, N. Rangarajan, U. Siddesh and C. N. R. Rao, Phys. Rev. B, 2006, **74**, 161306.
36. (a) D. Navas, J. Torrejon, F. Béron, C. Redondo, F. Batallan, B. P. Toperverg, A. Devishvili, B. Sierra, F. Castaño, K. R. Pirota and C. A. Ross, New J. Phys., 2012, 14, 113001; (b) W. J. Gong, W. Liu, X. H. Liu, S. Guo, J. N. Feng, B. Li and Z. D. Zhang, J. Appl. Phys., 2011, 109, 043906.
37. A. N. Dobrynin, D. N. Ievlev, K. Temst, P. Lievens, J. Margueritat, J. Gonzalo, C. N. Afonso, S. Q. Zhou, A. Vantomme, E. Piscopiello and G. Van Tendeloo, *Appl. Phys. Lett.* 2005, **87**, 012501.
38. H. Ohldag, A. Scholl, F. Nolting, E. Arenholz, S. Maat, A. T. Young, M. Carey and J. Stöhr, *Phys. Rev. Lett.* 2003, **91**, 017203.
39. R. F. L. Evans, R. W. Chantrell and O. Chubykalo-Fesenko, MRS Bulletin, 2013, 38, 909.
40. A. G. Kolhatkar, A. C. Jamison, D. Litvinov, R. C. Willson and T. R. Lee, *Int. J. Mol. Sci.*, 2013, **14**, 15977.

Table 1. Reaction parameters used in synthesis of monodisperse $Co_{0.33}Fe_{0.66}O$ NPs.

Run	Solvent (9 mL)	$CoFe_2$-oleate (mmol)	OA (mmol)	Temp. (C)	Time (min)	Size (nm)	ICP-MS (Fe/Co)
1	HDE	3	4	300	120	6.75 ±0.3	1.8
2	ODE	3	4	320	120	12.5 ±0.6	1.8
3	ODE	3	10	320	120	14.1±1.3	1.8
4	ESE	3	4	340	120	19.0±1.2	1.9

Table 2. Summary of refined Mössbauer parameters measured at 10 K: centroid shift (δ), quadrupole shift (ε), magnetic hyperfine field (B_{hf}), magnetic hyperfine distribution (σ), and intensities (*I*) of the different components.

Components	Parameters	Ambient oxidation	20-h expedited oxidation
	Size (nm)	12.5	12.5
Q_1	δ_1 (mm/s)	0.531	0.538
	ε_1 (mm/s)	0.052	0.050
	B_{hf} (mm/s)	52.5	53.1
	σ_1 (mm/s)	1.2	1.4
	I_1 (%)	19	24
Q_2	δ_2 (mm/s)	0.577	0.574
	ε_2 (mm/s)	-0.100	-0.102
	B_{hf} (mm/s)	51.3	51.8
	σ_2 (mm/s)	1.9	2.3
	I_2 (%)	24	29
Q_3	δ_3 (mm/s)	0.335	0.319
	ε_3 (mm/s)	0.010	0.021
	B_{hf} (mm/s)	50.2	51.1
	σ_3 (mm/s)	2.2	2.2
	I_3 (%)	33	41
Q_4	δ_4 (mm/s)	1.214	1.292
	ε_4 (mm/s)	-0.127	0.536
	B_{hf} (mm/s)	35.7	41.9
	σ_4 (mm/s)	11.7	9.9
	I_3 (%)	24	6

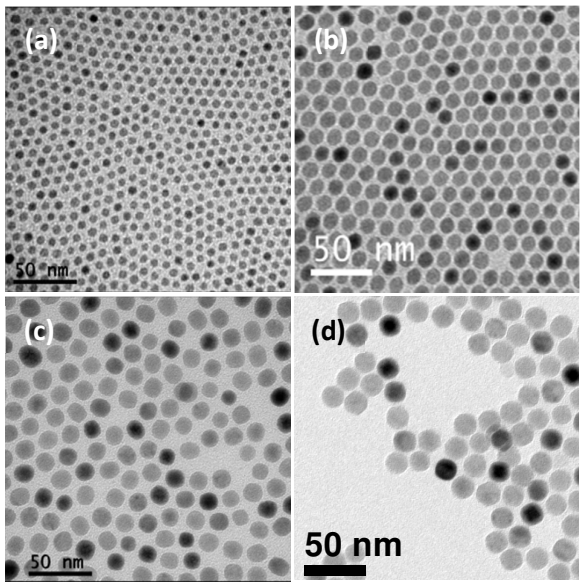

Figure 1. TEM images of monodisperse CWT NPs of different sizes: (a) 6.75 ± 0.3 nm, (b) 12.5 ± 0.6 nm, (c) 14.1 ± 1.3 nm, and (d) 19.0 ± 1.2 nm.

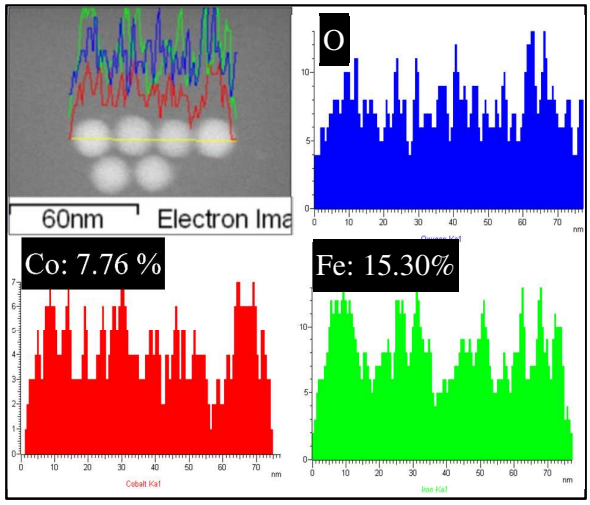

Figure 2. STEM micrographs of 19-nm CWT NPs showing spectrum lines and mean profiles with Fe and Co atomic %.

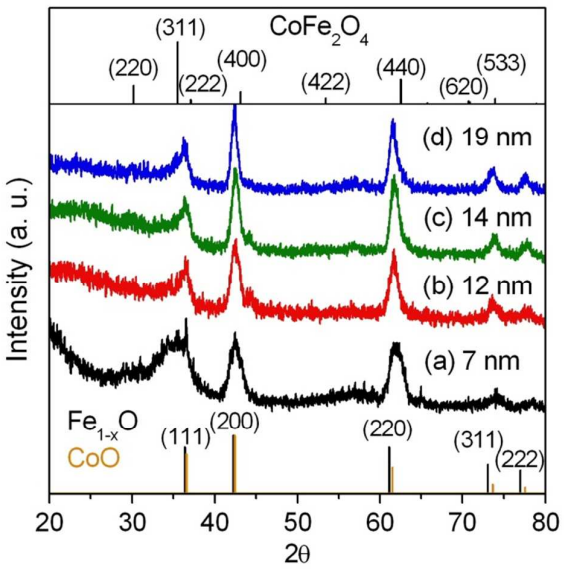

Figure 3. XRD patterns of CWT NPs of different sizes.

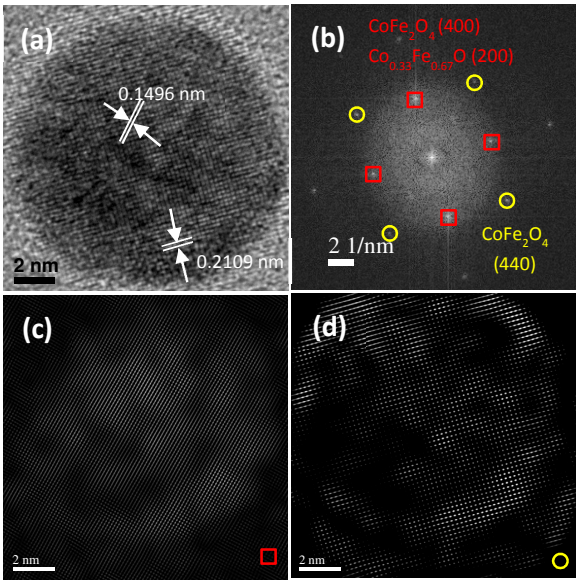

Figure 4. FFT analysis of 12.5-nm NPs following 120-day oxidation under ambient conditions. (a) HR-TEM image of selected NP. (b) FFT pattern constructed from lattice image in (a), where the spots marked with "□" correspond to (200) of $Co_{0.33}Fe_{0.66}O$ and (400) of $CoFe_2O_4$, while the spots marked with "O" correspond exclusively to (220) of $CoFe_2O_4$. (c) Image from the spots marked with "□". (d) Image from the spots marked with "O".

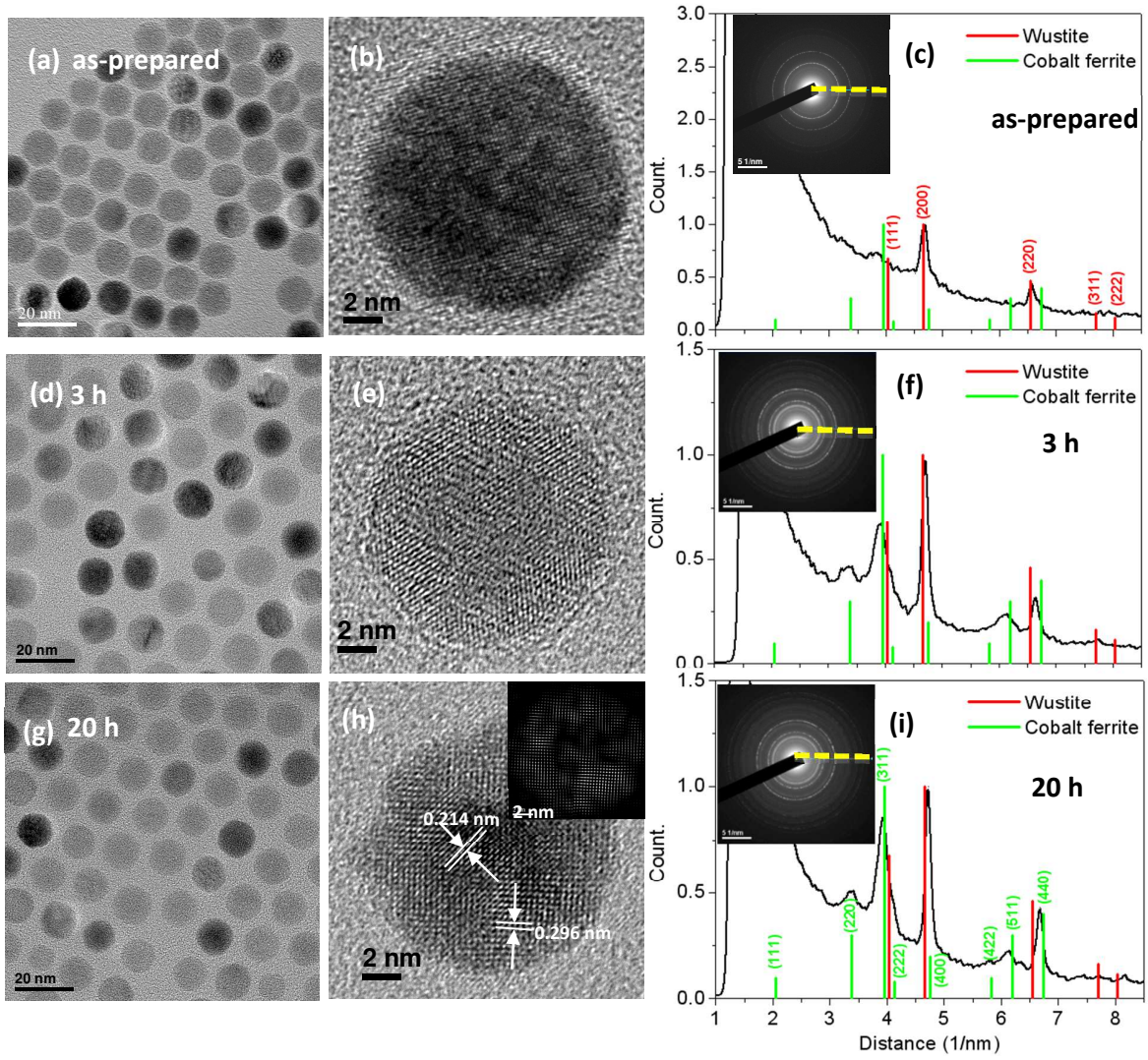

Figure 5. TEM and HRTEM micrographs, and line scan patterns obtained from SAED patterns of 12.5-nm CWT NPs before and after oxidation in TMNO solution. (a), (b) and (c) correspond to the as-prepared sample; (d), (e) and (f) correspond to the 3-h oxidized sample; (g), (h) and (i) correspond to the 20-h oxidized sample. Note that the inset in Fig. 5(h) shows the inverse FFT image reconstructed from the sole diffraction spot of $CoFe_2O_4$ in the 20-h oxidized sample.

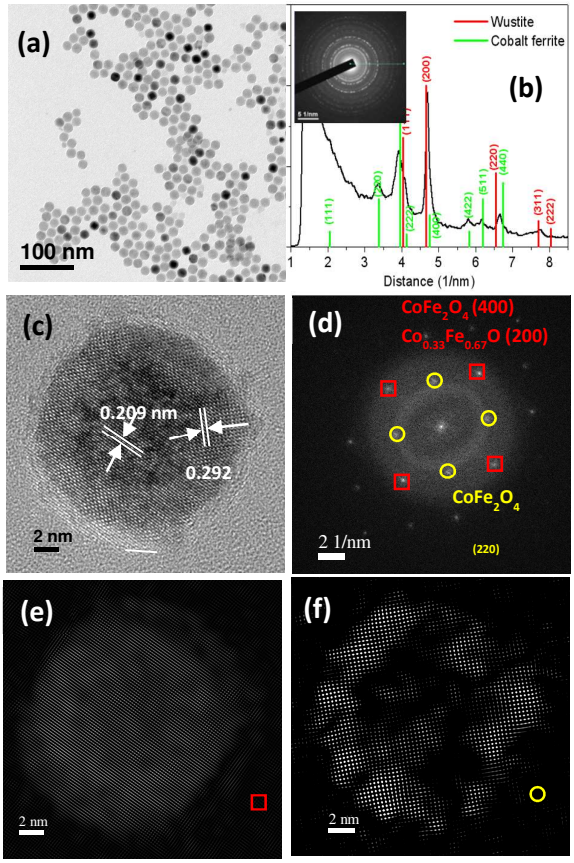

Figure 6. (a) TEM, (b) SAED patterns (inset) and line scan patterns, and (c) HRTEM micrographs of 19-nm $Co_{0.33}Fe_{0.67}O/CoFe_2O_4$ core-shell NPs. (d) FFT pattern obtained from lattice image in (c), where the spots marked with"□" correspond to (200) of $Co_{0.33}Fe_{0.66}O$ and (400) of $CoFe_2O_4$, while the spots marked with "O" correspond exclusively to (220) of $CoFe_2O_4$. (e) Image reconstructed from the spots marked with"□". (f) Image filtered reconstructed from the spots marked with "O".

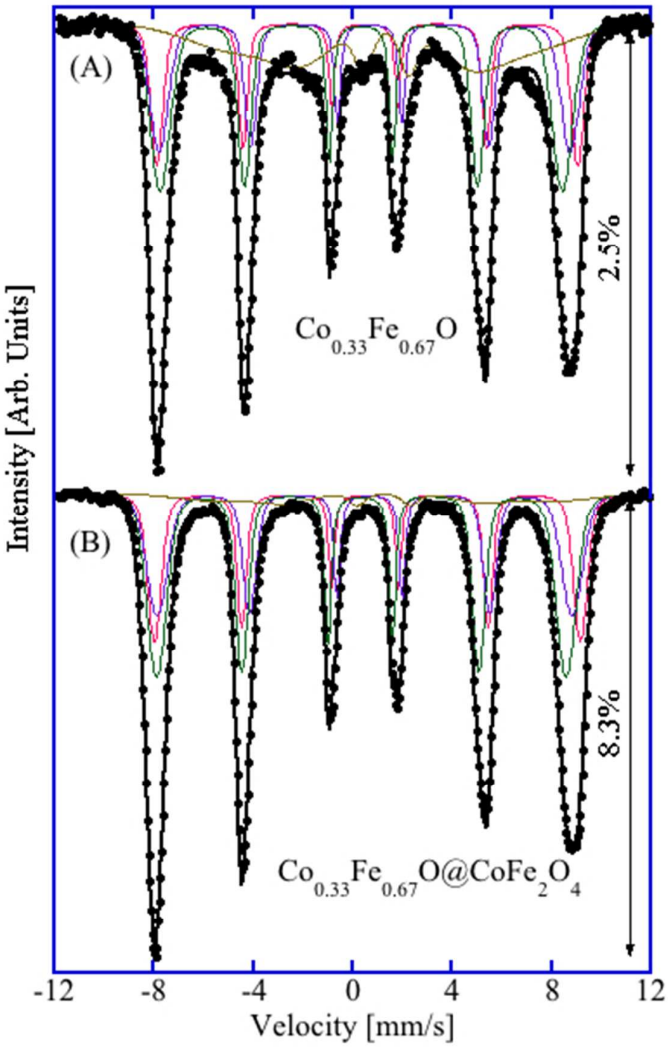

Figure 7. Mössbauer spectra for 12.5-nm samples measured at 10 K: (a) ambient oxidation and (b) 20-h expedited oxidation.

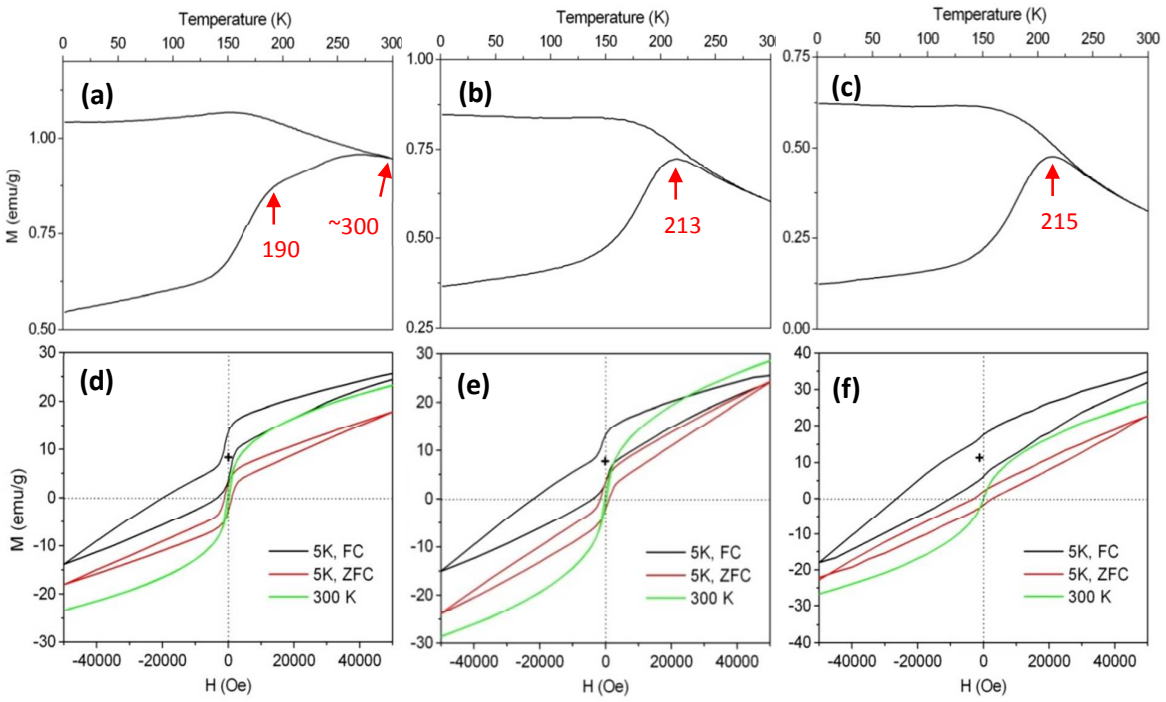

Figure 8. Temperature-dependent magnetization curves and hysteresis loops of 12.5-nm samples: (a, d) as-prepared NPs, (b, e) 30-d ambient oxidation, and (c, f) 120-d ambient oxidation.

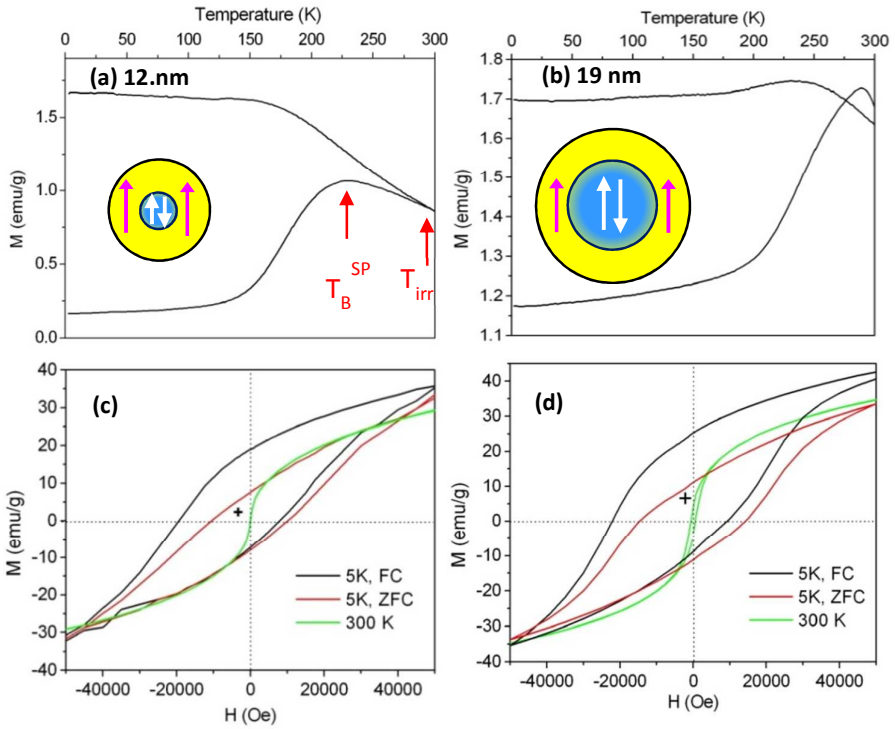

Figure 9. Temperature-dependent magnetization curves and hysteresis loops of NPs oxidized in TMNO solution at 160 °C for 20 h: (a, c) 12.5-nm sample, and (b, d) 19-nm sample.

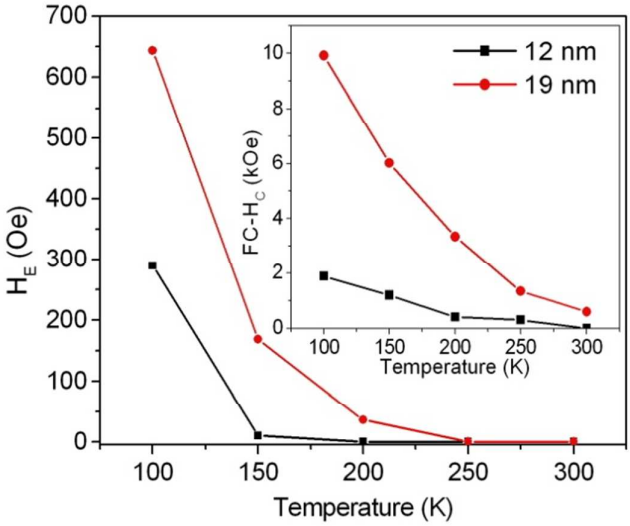

Figure 10. Temperature-dependent characteristics of exchange-bias field (H_E) and coercivity $H_{C,\,FC}$ of 12.5-nm and 19-nm samples oxidized in TMNO solution at 160 ^{o}C for 20 h.